Magnifying Quantum Phase Fluctuations with Cooper-Pair Pairing

W. C. Smith,[1,2,*] M. Villiers,[1,2] A. Marquet,[1,2] J. Palomo,[1] M. R. Delbecq,[1] T. Kontos,[1]
P. Campagne-Ibarcq,[2,1] B. Douçot,[3] and Z. Leghtas[4,1,2,†]

[1]*Laboratoire de Physique de l'Ecole Normale Supérieure, ENS, Université PSL, CNRS,
Sorbonne Université, Université Paris-Diderot, Sorbonne Paris Cité, Paris, France*
[2]*QUANTIC Team, Inria de Paris, 2 rue Simone Iff, 75012 Paris, France*
[3]*Laboratoire de Physique Théorique et Hautes Energies, Sorbonne Université and CNRS UMR 7589,
4 place Jussieu, 75252 Paris Cedex 05, France*
[4]*Centre Automatique et Systèmes, Mines-ParisTech, PSL Research University,
60 boulevard Saint-Michel, 75006 Paris, France*

Remarkably, complex assemblies of superconducting wires, electrodes, and Josephson junctions are compactly described by a handful of collective phase degrees of freedom that behave like quantum particles in a potential. Almost all these circuits operate in the regime where quantum phase fluctuations are small—the associated flux is smaller than the superconducting flux quantum—although entering the regime of large fluctuations would have profound implications for metrology and qubit protection. The difficulty arises from the apparent need for circuit impedances vastly exceeding the resistance quantum. Independently, exotic circuit elements that require Cooper pairs to form pairs in order to tunnel have been developed to encode and topologically protect quantum information. In this work, we demonstrate that pairing Cooper pairs magnifies the phase fluctuations of the circuit ground state. We measure a tenfold suppression of flux sensitivity of the first transition energy only, implying a twofold increase in the vacuum phase fluctuations and showing that the ground state is delocalized over several Josephson wells.

I. INTRODUCTION

In superconducting circuits, patterned electrodes are arranged in seemingly endless varieties to build hardware ranging from qubits to amplifiers [1,2]. Formally, their behavior reduces to that of a particle moving across corrugating Josephson potential wells superimposed on a parabolic background due to the circuit inductance. The finite particle mass, provided by the circuit capacitance, induces quantum fluctuations of the positionlike degree of freedom—the superconducting phase [3,4]. These circuits operate predominantly in the regime of small phase fluctuations, where the system ground state resides in a single potential well [5]. What would emerge from circuits whose ground states are delocalized among multiple Josephson wells?

[*]william.smith@ens.fr
[†]zaki.leghtas@ens.fr

Computational states that are spread in phase space over multiple sites are at the root of robust and hardware-efficient encoding of quantum information. In this scheme, the delocalization is engineered to combat, at the Hamiltonian level, the detrimental effects of noise stemming from local sources. The so-called grid states of the Gottesman-Kitaev-Preskill (GKP) error correction code and the 0-π qubit constitute notable examples [6,7]. In addition, such circuits could be tiled into topologically protected qubits [8] and employed for fault-tolerant error syndrome measurements [9,10], the development of quantum phase-slip elements [11], and the observation of Bloch oscillations [12]. Despite the wide scope of application, this regime remains largely inaccessible.

To understand this, consider a generic superconducting qubit that consists of an inductance, a capacitance, and a Josephson junction of energies $\mathcal{E}_L$, $\mathcal{E}_C$, and $\mathcal{E}_J$, respectively. Two parameters condition the regime of operation: $\mathcal{E}_J/\mathcal{E}_L$, which specifies the number of potential wells, and $\mathcal{E}_J/\mathcal{E}_C$, which determines the number of energy levels within a well. Here, the regime of interest corresponds to $\mathcal{E}_J/\mathcal{E}_C \sim 1$ and $\mathcal{E}_J/\mathcal{E}_L \gg 1$, implying $\mathcal{E}_C/\mathcal{E}_L \gg 1$. The latter condition corresponds to a linear circuit with characteristic impedance far exceeding the superconducting resistance quantum, which constitutes a formidable challenge. Initial

progress was made using the advent of the superinductance [13], now realized in various materials [14–17]. However, surpassing this threshold by 2 orders of magnitude has only recently been achieved in a feat of nanofabrication, where Josephson junction arrays are suspended in vacuum [18].

On the other hand, in the area of topologically protected Josephson qubits [8], quantum information is robustly encoded in the highly degenerate ground state manifold of a fabric of circuit elements. The workhorse of these circuits is an exotic junction that forbids single Cooper-pair tunneling by Aharonov-Bohm interference, allowing only pairs of Cooper pairs to tunnel and resulting in an inherent twofold ground state degeneracy [19,20].

In this article, we demonstrate that pairing Cooper pairs magnifies quantum phase fluctuations. This enhancement originates from the cancellation of single Cooper-pair tunneling, which is a significant departure (but not mutually exclusive) from the common technique of increasing the length of a kinetic inductance. We accomplish this using a generalized Josephson element, which can be tuned *in situ* between two operating points where the potential is 2π or π periodic [21,22]. This doubles the frequency of the corrugation and, hence, also the number of sites accessible to the ground state. We refer to this change of scale, resulting from a denser packing of the Josephson wells, as a magnification. In our experimental realization, we shunt this generalized Josephson element with a conventional superinductance and measure the low-lying transition energies as a function of the external magnetic flux threading the loop. We observe a tenfold suppression of the dispersion of the first excited transition energy in flux, corresponding to a twofold increase in the quantum fluctuations of the phase, which essentially washes out the effects of localization.

II. TOY MODEL

The lumped element circuit we aim to implement [represented in Fig. 1(a)] is described by the Hamiltonian

$$\mathcal{H}_\mu = 4\mathcal{E}_C\left(\frac{N}{\mu}\right)^2 + \frac{1}{2}\mathcal{E}_L(\varphi - \varphi_{\text{ext}})^2 + (-1)^\mu \mathcal{E}_J \cos(\mu\varphi).$$

$$(1)$$

Here, φ is the gauge-invariant superconducting phase drop across the generalized Josephson element, and N is the conjugate number of tunneled Cooper pairs. The external magnetic flux threading the loop is φ_{ext} (in dimensions of phase), and the parameter $\mu = 1, 2, \ldots$ specifies the multiplicity of Cooper pairs that tunnel, as can be seen in the charge basis:

$$\cos(\mu\varphi) = \frac{1}{2}\sum_{N=-\infty}^{\infty}(|N\rangle\langle N+\mu| + |N+\mu\rangle\langle N|). \quad (2)$$
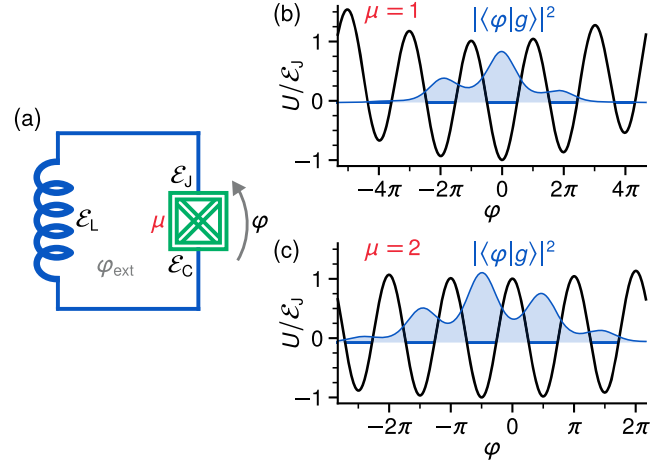

FIG. 1. Principle of magnifying the quantum phase fluctuations. (a) Electrical circuit diagram for a generalized Josephson junction (cross-hatched box) shunted by a superinductance. This junction possesses an internal parameter $\mu = 1, 2, \ldots$ that specifies the periodicity of the Josephson potential. (b),(c) Potential and ground state probability density for the cases $\mu = 1$ and $\mu = 2$ at $\varphi_{\text{ext}} = \pi/3$, showing the increase in the number of Josephson wells accessible to the ground state.

Note the occurrence of μ in the charging term in Eq. (1), motivated by our particular implementation and to keep the generalized Josephson element plasma frequency constant. The $(-1)^\mu$ factor guarantees that the cosine potential is pinned to 1 at $\pm\pi$ for all μ. In the fluxonium regime $\mathcal{E}_L \ll \mathcal{E}_C \lesssim \mathcal{E}_J$, the ground state is confined to the lowest few potential wells [13]. When the period of the Josephson potential is halved by changing $\mu = 1$ to $\mu = 2$, the ground state delocalization is substantially magnified [see Figs. 1(b) and 1(c)].

To see this another way, in the rescaled coordinates $\varphi \to \varphi/\mu$ and $N \to \mu N$, the amplitude of the zero-point fluctuations of the phase across the generalized Josephson element is given by

$$\varphi_{\text{zpf}} = \left(\frac{2\mathcal{E}_C}{\mathcal{E}_L}\mu^2\right)^{1/4}. \quad (3)$$

Incrementing μ from one to two magnifies φ_{zpf} by a factor $\sqrt{2}$. Putting this into perspective, this is the enhancement that would be obtained from reducing the stray capacitance in a Josephson junction array by a factor of 16, allowing a fourfold increase in the total linear inductance, a strategy followed by Ref. [18]. Interestingly, recasting $\sqrt{\mathcal{E}_C/\mathcal{E}_L}$ in Eq. (3) in terms of the ratio of circuit impedance Z_0 to vacuum impedance Z_{vac} yields

$$\varphi_{\text{zpf}} = \sqrt{8\pi\alpha\mu\frac{Z_0}{Z_{\text{vac}}}}, \quad (4)$$

where $\alpha \approx 1/137$ is the fine structure constant. Regarding the shunting circuit and vacuum impedances as independent of μ indicates that, here, the magnified fine structure constant $\alpha \times \mu$ for pairs of Cooper pairs appears twice as large as for Cooper pairs. This analogy provides insight into a world where charge and phase fluctuations naturally occur at the same scale. Indeed, the ratio of flux fluctuations (relative to Φ_0) and charge fluctuations (relative to $2e$) is on the scale of 8 times the fine structure constant [23]. In contrast, in a circuit where electrons can move only in packets of μ Cooper pairs, one finds that the ratio of flux to charge fluctuations gains a factor of μ. Taking $\mu = 1/(8\alpha) \approx 17$, one obtains a circuit where charge and flux fluctuate on similar scales.

III. CIRCUIT IMPLEMENTATION

Our implementation of the generalized Josephson element follows the proposal of Ref. [24] [see the green portion in Fig. 2(a)]. A superconducting loop is composed of two nearly identical small Josephson junctions, with tunneling energy E_J and charging energy E_C, in parallel and each in series with a superinductance with inductive energy $\epsilon_L \ll E_J$. In contrast with the rhombus [21], we name this dipole element the kinetic interference cotunneling element (KITE). Unlike the rhombus, the KITE does not contain any isolated superconducting islands and is, therefore, immune to offset charge noise [22,25]. An additional advantage of the KITE is the reduced sensitivity
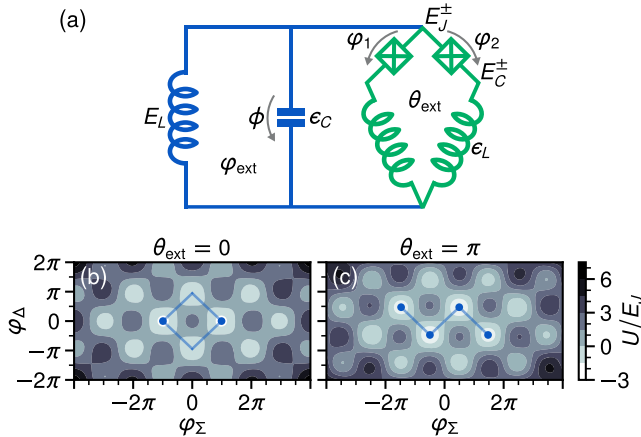

FIG. 2. Schematic of the experimental device. (a) Electrical circuit diagram for the KITE (green) shunted by a superinductance and a capacitance (blue). Additionally, the two small Josephson junctions are allowed to have slightly differing areas, so $E_J^\pm = (1 \pm \epsilon)E_J$ and $E_C^\pm = E_C/(1 \pm \epsilon)$, with ϵ being a small asymmetry parameter. (b),(c) Potential energy landscape at the external flux bias points $\varphi_{\text{ext}} = \pi$ and $\theta_{\text{ext}} = 0, \pi$. Here, φ_Σ and φ_Δ are the symmetric and antisymmetric combinations, respectively, of the phase drops across the two junctions of the KITE. The low-energy physics is dominated by tunneling (semitransparent blue segments) between the lowest potential wells (solid blue dots).

to flux noise within the loop owing to the large internal inductance. The KITE behaves like the generalized Josephson element depicted in Fig. 1(a) with $\mu = 1$ at the threaded external flux value $\theta_{\text{ext}} = 0$ and $\mu = 2$ at $\theta_{\text{ext}} = \pi$, which we hereafter refer to as zero and half flux, respectively. While a single ridge of potential wells at zero flux leads to a spacing of 2π in the symmetric phase φ_Σ between adjacent minima [see Fig. 2(b)], two ridges are interleaved at half flux, reducing the spacing to π [see Fig. 2(c) and Appendix B] [26]. Physically, this corresponds to the complete destructive Aharonov-Bohm interference of single Cooper-pair tunneling between the two arms of the KITE at half flux. We shunt the KITE with a superinductance (blue) of inductive energy E_L and its associated capacitance of charging energy ϵ_C. The parameter regime that we operate in is $E_L < \epsilon_L \ll E_J \sim E_C$. All superinductances are implemented with Josephson junction arrays, and ϵ_C is determined by the specific geometric arrangement of the connection wires.

IV. CIRCUIT QUANTIZATION

The circuit in Fig. 2(a) has three degrees of freedom: two corresponding to the KITE and one to the shunting circuit. We obtain the Hamiltonian [3]

$$
\begin{aligned}
H = {} & \frac{2E_C}{1-\epsilon^2}(N_\Sigma^2 + N_\Delta^2 - 2\epsilon N_\Sigma N_\Delta) + 4\epsilon_C n^2 + \frac{1}{2}E_L\phi^2 \\
& + \epsilon_L\left(\phi - \varphi_\Sigma - \varphi_{\text{ext}} - \frac{1}{2}\theta_{\text{ext}}\right)^2 + \epsilon_L\left(\varphi_\Delta - \frac{1}{2}\theta_{\text{ext}}\right)^2 \\
& - 2E_J\cos\varphi_\Sigma\cos\varphi_\Delta + 2\epsilon E_J\sin\varphi_\Sigma\sin\varphi_\Delta,
\end{aligned}
\tag{5}
$$

where ϵ is a small junction asymmetry parameter. Because of the high degree of symmetry in the KITE, we introduce the symmetric and antisymmetric variables $\varphi_\Sigma = \frac{1}{2}(\varphi_1 + \varphi_2)$ and $\varphi_\Delta = \frac{1}{2}(\varphi_1 - \varphi_2)$, respectively, in the above. Note also that $\{N_\Sigma, N_\Delta, n\}$ are the conjugate Cooper-pair numbers to $\{\varphi_\Sigma, \varphi_\Delta, \phi\}$. Numerical diagonalization of Eq. (5) is readily carried out in the three-mode Fock basis [27].

Our analysis focuses on the regime where ϵ_C is the dominant energy scale, so we proceed by applying the Born-Oppenheimer approximation to project the ϕ mode into its ground state and obtain a Hamiltonian depending only on φ_Σ and φ_Δ (see Appendix B). Afterward, since E_J is the largest remaining energy scale, we adopt a two-dimensional tight-binding model. At the bias point $\theta_{\text{ext}} = \pi$, this model can be further mapped to the one-dimensional continuous Hamiltonian

$$
H_\pi = 4E_C\left(\frac{N}{2}\right)^2 + \frac{E_L\epsilon_L}{E_L + 2\epsilon_L}(\varphi + \varphi_{\text{ext}})^2 + E_J\cos 2\varphi,
\tag{6}
$$

where φ approximately follows the degree of freedom φ_Σ, which, in turn, approximately follows ϕ in the limit of $E_L \ll \epsilon_L$ (see Appendix B). We also define the magnified

amplitude of zero-point fluctuations of the superconducting phase [4]:

$$\varphi_{zpf,\pi} = \left(8E_C \frac{E_L + 2\epsilon_L}{2E_L\epsilon_L}\right)^{1/4}. \qquad (7)$$

On the other hand, at the bias point $\theta_{ext} = 0$, this model can be mapped to

$$H_0 = 4\tilde{E}_C N^2 + \frac{E_L\epsilon_L}{E_L + 2\epsilon_L}(\varphi + \varphi_{ext})^2 - \tilde{E}_J \cos\varphi, \qquad (8)$$

where $\tilde{E}_J$ and $\tilde{E}_C$ are effective Josephson and charging energies, respectively, that are not readily cast in terms of the other circuit parameters. Again, we define the amplitude of zero-point fluctuations of the phase

$$\varphi_{zpf,0} = \left(2\tilde{E}_C \frac{E_L + 2\epsilon_L}{2E_L\epsilon_L}\right)^{1/4}. \qquad (9)$$
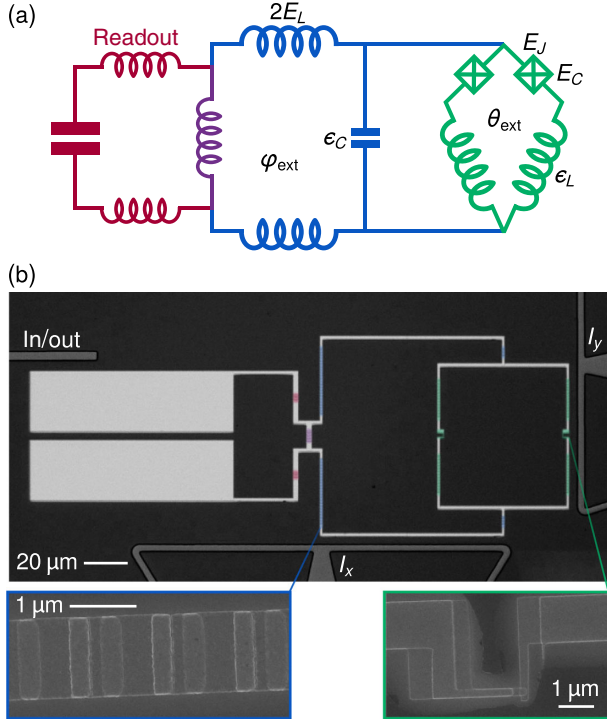

(a)

(b)

FIG. 3. Experimental implementation. (a) Extended electrical circuit diagram for the inductively shunted KITE including the lumped LC oscillator (maroon) added for dispersive readout, which couples inductively to the circuit through a shared inductance (purple). (b) Optical micrograph of the physical device, with aluminum electrodes in light gray and niobium electrodes in dark gray. Direct currents, microwave drives, and readout signals are routed in and out of the system through two on-chip flux bias lines (right and bottom) and one weakly coupled pin (top left). Insets: scanning electron microscope images of one array of large junctions [all inductances pictured in (a) are implemented similarly] and one small junction.

We complete the connection between our experimental circuit and the desired model by observing that Eqs. (6) and (8) map directly onto Eq. (1) in the cases of $\mu = 2$ and $\mu = 1$, respectively.

V. EXPERIMENTAL REALIZATION

The circuit in Fig. 2(a) is measured through a lumped LC readout resonator (maroon), which is coupled through a shared inductance (purple) as shown in Fig. 3(a). We fabricate the circuit by first sputtering niobium over a silicon substrate to define the control lines [see Fig. 3(b)]. Then, a double-angle aluminum evaporation step produces the two small junctions and the 100 total large junctions of the KITE, as well as the 100 large junctions of the shunting
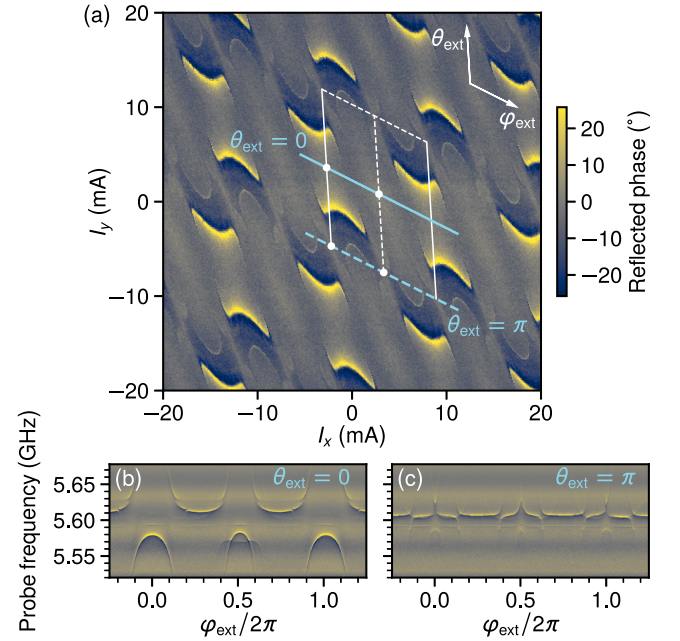

FIG. 4. Device flux dependence. (a) Phase of the reflected probe signal (color) on the readout port, at the fixed probe frequency of 5.595 GHz, as a function of both flux bias currents I_x and I_y. The overlaid lines indicate the independent φ_{ext} and θ_{ext} axes, while dots mark points of inversion symmetry. This phase response signals the periodic approach of the circuit transition energies in the vicinity of the readout resonance. (b),(c) Phase of the reflected probe signal (color) on the readout port, as a function of probe frequency and external flux φ_{ext} at zero and half flux [solid and dashed blue lines in (a)], displaying periodic avoided crossings.

superinductance. The number of superinductance junctions is chosen to keep all the self-resonant array modes above 10 GHz [28]. We extract the circuit parameters listed in Table I. The device is then measured in a dilution refrigerator at 10 mK.

We observe the phase response of the readout resonator [see Fig. 4(a)], which is periodically repelled by transition energies of the circuit [see Figs. 4(b) and 4(c)], as we sweep the on-chip flux bias currents [29]. Each of the small KITE junctions contributes a cosinusoidal Josephson potential, resulting in a circuit Hamiltonian that is 2π periodic in both loop fluxes and symmetric about the points $(\varphi_{\text{ext}}, \theta_{\text{ext}}) = (0, 0)$, $(\pi, 0)$, $(0, \pi)$, and (π, π) [see Eq. (5)]. These symmetries are observed in the data in Fig. 4(a), where we trace the primitive cell closest to the zero-bias point (overlaid lines), which sets the scale and angle of the φ_{ext} and θ_{ext} axes. The mapping between the flux bias currents (I_x, I_y) and $(\varphi_{\text{ext}}, \theta_{\text{ext}})$ is completed by identifying the four points of inversion symmetry within the primitive cell (solid white dots) and labeling them based on the fine energy structure of the system.

VI. TRANSITION ENERGIES

We access the transition energies of the circuit in a two-tone spectroscopy experiment at $\theta_{\text{ext}} = 0, \pi$ [see Figs. 5(c)

and 5(d)]. For each external flux value φ_{ext}, we calibrate the frequency of a readout tone and measure its reflected phase response as a function of the frequency of a probe tone fed into the I_x port. In order to fully constrain the circuit Hamiltonian identification, we report the fitted center frequencies of all persistent spectral lines visible below 6.6 GHz. We fit the 12 measured transition energies (five at zero flux and seven at half flux) to the eigenspectrum of the Hamiltonian in Eq. (5), parametrized by $\{E_J, E_C, E_L, \epsilon_L\}$ (see Appendix C). The remarkable agreement between data and theory is a powerful demonstration that this relatively complex assembly—involving two loops and 215 Josephson junctions—is well captured by a three-mode model with only four independent parameters.

The most essential feature of this spectrum is the drastic reduction of the flux dispersion of the first excited state transition, which spans 1.6 GHz at zero flux and only 140 MHz at half flux [blue circles in Figs. 5(c) and 5(d)]. Since the higher transitions exhibit significant flux dependence, this reduction is a direct signature of the ground and first excited state delocalization over additional Josephson wells. Indeed, as the external flux is increased, the cosinusoidal corrugation slides over the parabolic background. A particle localized in a single Josephson well—known as a fluxon state—is carried upward in energy until it tunnels to the trailing descending fluxon state, resulting in a large flux
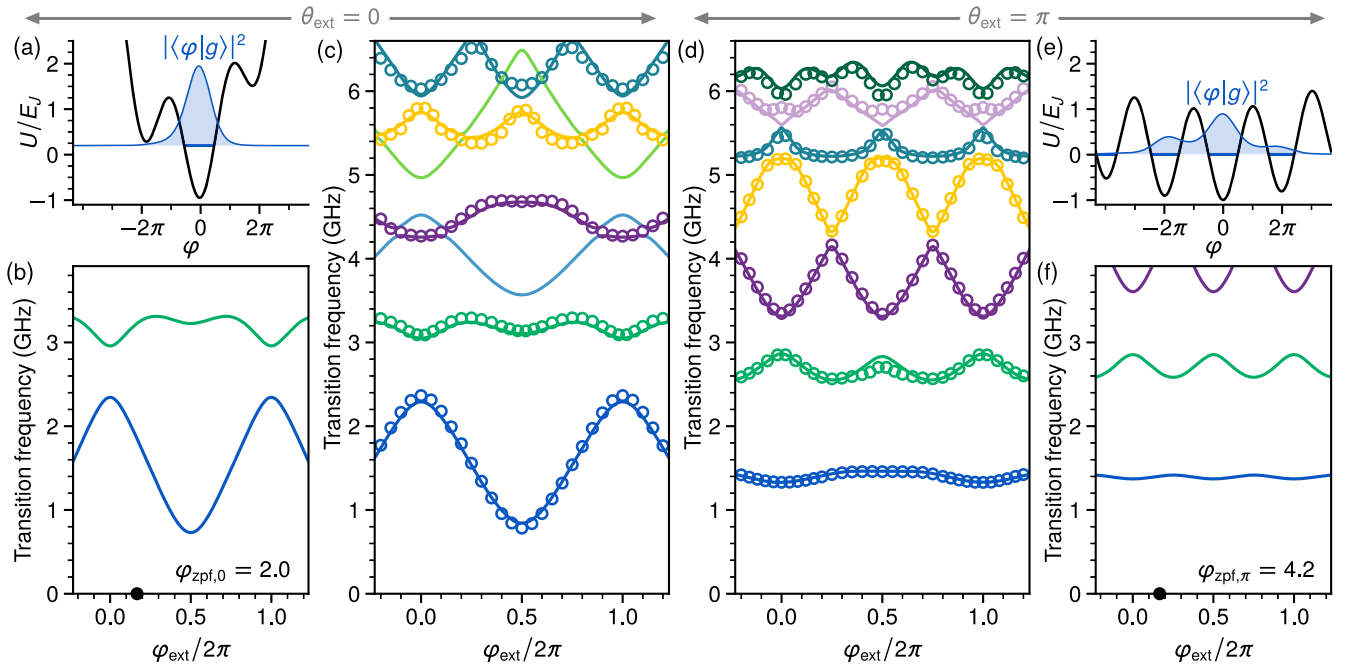

FIG. 5. Magnified quantum phase fluctuations. (a),(e) Potential energy landscape and ground state probability density at $\varphi_{\text{ext}} = \pi/3$ (black dot in plots beneath) for the cases of zero flux $\theta_{\text{ext}} = 0$ and half flux $\theta_{\text{ext}} = \pi$. (b),(f) Lowest-lying transition frequencies of the effective single-mode Hamiltonians at zero and half flux in Eqs. (8) and (6) with parameters in Table I, showing an increase in the amplitude of the zero-point fluctuations of the phase from $\varphi_{\text{zpf},0} = 2.0$ to $\varphi_{\text{zpf},\pi} = 4.2$. (c),(d) Two-tone measurements of the transition frequencies from the ground state (open circles) and corresponding fitted values (solid curves) obtained from the three-mode circuit. The light blue and light green transitions are not visible in spectroscopy due to their strong decoupling from the readout resonator. The essential feature is the remarkable suppression of flux dispersion of the first excited state transition when θ_{ext} is stepped from 0 to π.

dispersion. On the other hand, a delocalized particle simultaneously occupies ascending and descending fluxon states, washing out the flux dependence of the energy.

An additional striking feature of Fig. 5(d) is the dominant π periodicity of the energy spectrum at $\theta_{\text{ext}} = \pi$, in stark contrast with the usual 2π periodicity of a Josephson potential, as observed in Fig. 5(c). This effect is slightly diminished by residual asymmetry in the areas of the two small KITE junctions, which we find to be around 6%. Finally, note the two transitions at zero flux [light blue and light green lines in Fig. 5(c)] predicted by theory but not observed in the experiment. This is explained by the vanishingly small dispersive coupling of these transitions to the readout resonator, as predicted by circuit quantization [30].

Although a three-mode model is necessary to capture the complete energy spectrum up to 6.6 GHz, the first few transition energies are well described by the emergent low-energy Hamiltonians of Eqs. (8) and (6) with parameters listed in Table I, as shown in Figs. 5(b) and 5(f). Note that in the experiment we observe a magnification factor of $\varphi_{\text{zpf},\pi}/\varphi_{\text{zpf},0} = 2.1$, which is larger than the factor of $\sqrt{2}$ predicted by Eq. (3), because the effective behavior of our circuit at $\theta_{\text{ext}} = 0$ involves double-phase-slip processes (see Appendix B). We find $\varphi_{\text{zpf},\pi} = 4.2 \pm 0.2$, which is strictly larger than π, therefore unambiguously placing our system in the regime of ground state delocalization.

VII. OUTLOOK

An ongoing quest in quantum information science is to build a circuit that hosts a degenerate ground state manifold that encodes and protects quantum states. A particularly appealing approach is to combine a generalized Josephson element with the so-called quantum phase-slip element [11], the dual of the Josephson junction [31]. Such a circuit would encode information in the form of GKP states [6] that are protected at the Hamiltonian level, circumventing the need for error syndrome measurements and feedback. The key technological innovation of our experiment—the KITE—is an implementation of such a generalized Josephson element. This circuit would then need to be combined with additional parts that effectively play the role of a phase-slip element. We are then confronted with the usual challenge in quantum error correction, where adding complexity to a circuit may have the virtue of hosting a protected manifold of states but comes at the cost of adding error channels. Examples are charge noise in each added island and flux noise in each added loop. Inventing a circuit where the protection overcomes all these additional sources of errors is an active area of research [32].

VIII. CONCLUSION

In conclusion, we have built a superconducting circuit whose ground state wave function spreads across multiple

Josephson potential wells by packing them closer together via Cooper-pair pairing. We refer to this process as magnification of the phase fluctuations and quantify it by an amplitude $\varphi_{\text{zpf},\pi} = 4.2 \pm 0.2$. We find it intriguing that the origin of this phenomenon does not rely on the inertia (kinetic inductance) of charge carriers but by forcing them to tunnel in pairs. We envision incorporating a quantum phase-slip element into our circuit to implement a protected qubit, observe the quantum dynamics of non-local operators, and perform fault-tolerant error syndrome measurements [9,10].

W. C. S. conceived the experiment and measured the device. W. C. S., assisted by A. M., designed the sample. Z. L. fabricated the sample. W. C. S., Z. L., B. D., and P. C.-I. analyzed the data. M. V., J. P., T. K., and M. R. D. provided experimental support. W. C. S. and Z. L. cowrote the manuscript with input from all authors.

APPENDIX A: DEVICE FABRICATION

The circuit is fabricated on a 280-μm-thick wafer of intrinsic silicon (resistivity exceeding $10\,000\;\Omega\,\text{cm}$). The silicon wafer is cleaned in solvents and loaded in a sputtering system. After one night of pumping, we start with an argon milling cleaning step and proceed to sputter 120 nm of niobium onto the chip. We spin optical resist (S1805) and pattern the large features (control lines) with a laser writer. After development (MF319), we etch the sample in SF6 with a 20-s overetch, followed by lift off (acetone at $50\,°\text{C}$). We then spin a bilayer of MAA (EL11) and PMMA (A6). The entire circuit (KITE, inductive shunt, and readout resonator) is patterned in an *e*-beam lithography step. The development takes place in a $3\!:\!1$ IPA/water solution at $6\,°\text{C}$ for 90 s, followed by 10 s in IPA. The chip is then loaded in an *e*-beam evaporator. We start with a thorough argon ion milling for 2 min with the sample at the angles of 0° and 45°, which serves the purpose of cleaning the substrate. We then evaporate 35 and 70 nm of aluminum, at 0° and 45° angles, separated by an oxidation step of 200 mbar of pure oxygen for 10 min.

The Josephson junctions are all fabricated from Al/AlOx/Al in a single evaporation step, using the Dolan bridge method with an *e*-beam base dose of $283~\mu\text{C}\,\text{cm}^{-2}$ at an acceleration voltage of 20 kV, and come in three types: (i) two small junctions in the KITE of area $0.075~\mu\text{m}^2$, made in a cross geometry, patterned with a dose factor of 1.6, and resulting in an inductance per junction of 52 nH; (ii) a total of 100 large array junctions within the KITE loop and a total of 100 unshared shunting array junctions, of area $0.49~\mu\text{m}^2$, patterned with a dose factor of 1.8, and resulting in an inductance per junction of 6.8 nH; and (iii) 13 larger array junctions that form the readout resonator inductance (seven of which are shared) of area $1.10~\mu\text{m}^2$, patterned with a dose factor of 1.5, and resulting in an inductance per junction of 3.45 nH.

The chip is subsequently baked at $115\,^\circ\text{C}$ for 1 min, glued with PMMA onto a PCB, wire-bonded, and mounted into a sample holder. The device is then thermally anchored to the base plate of a Bluefors dilution refrigerator, surrounded by three concentric cans for magnetic and infrared shielding (outer, cryoperm; middle, aluminum; inner, copper). An optical micrograph of the circuit and SEM images of some junctions are shown in Fig. 3(b).

APPENDIX B: MODEL REDUCTION

In this section, we describe the mathematical procedure for reducing the three-mode Hamiltonian in Eq. (5) to an effective one-mode Hamiltonian at the KITE bias values $\theta_{\text{ext}} = \pi, 0$. The main purpose of these approximations is to extract an effective amplitude of quantum phase fluctuations and, thereby, benchmark the extent of observed ground state delocalization.

1. Born-Oppenheimer approximation

We first define the energy scales of the circuit according to

$$E_C = \frac{e^2}{2C_J}, \qquad \epsilon_C = \frac{e^2}{2C}, \qquad E_J = \frac{\phi_0^2}{L_J},$$
$$E_L = \frac{\phi_0^2}{L}, \qquad \epsilon_L = \frac{\phi_0^2}{\ell}, \tag{B1}$$

where $\phi_0 = \hbar/2e$ is the reduced magnetic flux quantum, and we place ourselves in the regime where $E_L < \epsilon_L \ll E_J \sim E_C$ and $\epsilon \ll 1$ in Eq. (5). Furthermore, we are chiefly interested in the limit where ϵ_C is the dominant energy scale, i.e., the limit of small shunt capacitance. While we do not strictly achieve this experimentally due to our specific circuit geometry, this limit conveniently reveals the relevant underlying physics of the circuit. In Born-Oppenheimer theory, one considers a system with a collection of high-frequency electronlike degrees of freedom and a collection of low-frequency nucleuslike degrees of freedom. To obtain

an approximate Hamiltonian for the "nuclei," one freezes the "electrons" in their quantum ground state, which is found by fixing the nuclear variables to their classical values. In our system, we regard the ϕ variable as high frequency and treat the φ_Σ and φ_Δ variables as low frequency. Fixing φ_Σ and φ_Δ to their classical values and setting N_Σ and N_Δ to zero, Eq. (5) reduces to

$$H_e = 4\epsilon_C n^2 + \frac{1}{2}E_L\phi^2 + \epsilon_L\left(\phi - \varphi_\Sigma - \varphi_{\text{ext}} - \frac{1}{2}\theta_{\text{ext}}\right)^2. \tag{B2}$$

Note that, in this equation, ϕ and n are operators, while φ_Σ is a parameter. This Hamiltonian simply describes a harmonic oscillator whose equilibrium position is $\langle\phi\rangle = [2\epsilon_L/(E_L + 2\epsilon_L)](\varphi_\Sigma + \varphi_{\text{ext}} + \frac{1}{2}\theta_{\text{ext}})$. In the limit that $E_L \ll \epsilon_L$, we observe that the dynamics of ϕ rigidly follow those of φ_Σ. We can, hence, readily identify the energy levels of H_e as

$$E_{e,m} = \sqrt{8(E_L + 2\epsilon_L)\epsilon_C}\left(m + \frac{1}{2}\right)$$
$$+ \frac{E_L\epsilon_L}{E_L + 2\epsilon_L}\left(\varphi_\Sigma + \varphi_{\text{ext}} + \frac{1}{2}\theta_{\text{ext}}\right)^2. \tag{B3}$$

We may then plug this into Eq. (5) to obtain the effective low-energy Hamiltonian

$$H_n = \frac{2E_C}{1-\epsilon^2}(N_\Sigma^2 + N_\Delta^2 - 2\epsilon N_\Sigma N_\Delta)$$
$$+ \frac{E_L\epsilon_L}{E_L + 2\epsilon_L}\left(\varphi_\Sigma + \varphi_{\text{ext}} + \frac{1}{2}\theta_{\text{ext}}\right)^2 + \epsilon_L\left(\varphi_\Delta - \frac{1}{2}\theta_{\text{ext}}\right)^2$$
$$- 2E_J\cos\varphi_\Sigma\cos\varphi_\Delta + 2\epsilon E_J\sin\varphi_\Sigma\sin\varphi_\Delta$$
$$+ \sqrt{8(E_L + 2\epsilon_L)\epsilon_C}\left(m + \frac{1}{2}\right). \tag{B4}$$

Recall that, here, φ_Σ and φ_Δ are restored as operators (as well as N_Σ and N_Δ), while ϕ is reduced to the discrete parameter $m = 0, 1, \dots$ (playing the role of an orbital index) while also modifying the energy landscape of φ_Σ. Note that the solutions to H_n can be expected to resemble those to the full Hamiltonian only for energies smaller than $\sqrt{8(E_L + 2\epsilon_L)\epsilon_C}$. For our experimental parameters, this cutoff corresponds to a frequency of 4.35 GHz, which makes this analysis relevant for the first two transitions only. Furthermore, the inductive energy for φ_Σ corresponds to that for a series arrangement of inductances L and $\ell/2$ (a parallel arrangement of two inductances ℓ).

2. Projection at $\theta_{\text{ext}} = \pi$

Restricting our attention to the case of symmetric junctions, we consider Eq. (B4) for $m = 0$:

$$H_{n,\pi} = 2E_C(N_\Sigma^2 + N_\Delta^2) + \frac{E_L \epsilon_L}{E_L + 2\epsilon_L}(\varphi_\Sigma + \varphi_{\text{ext}})^2 + \epsilon_L \varphi_\Delta^2$$
$$+ 2E_J \sin\varphi_\Sigma \sin\varphi_\Delta. \tag{B5}$$

Since E_J is the dominant energy scale, we first consider the locations at which the Josephson tunneling energy is minimized: $\varphi_\Sigma = (m_\Sigma + \frac{1}{2})\pi$ and $\varphi_\Delta = (m_\Delta + \frac{1}{2})\pi$, where

m_Σ and m_Δ are integers with the same parity. Because of their small energy scales, the linearly inductive terms contribute only a broad parabolic confinement centered at $\varphi_\Sigma = -\varphi_{\text{ext}}$ and $\varphi_\Delta = 0$. It is then natural to introduce a two-dimensional tight-binding model with individual sites corresponding to the different Josephson wells. To this end, we arrive at the Hamiltonian

$$H_{n,\pi}^{\text{tight-binding,2D}} = \sum_{\{m_\Sigma + m_\Delta \text{even}\}} \left[\frac{E_L \epsilon_L}{E_L + 2\epsilon_L}\left(m_\Sigma \pi + \frac{\pi}{2} + \varphi_{\text{ext}}\right)^2 + \epsilon_L\left(m_\Delta \pi + \frac{\pi}{2}\right)^2 \right] |m_\Sigma, m_\Delta\rangle\langle m_\Sigma, m_\Delta|$$
$$- \sum_{\{m_\Sigma + m_\Delta \text{even}\}} \frac{1}{2}\Gamma(|m_\Sigma, m_\Delta\rangle\langle m_\Sigma \pm 1, m_\Delta \pm 1| + |m_\Sigma \pm 1, m_\Delta \pm 1\rangle\langle m_\Sigma, m_\Delta|), \tag{B6}$$

where the index $\{m_\Sigma + m_\Delta \text{even}\}$ indicates summation over only the lowest potential minima and the hopping energy Γ corresponds to the nearest-neighbor tunneling rate for the lowest wells. The factor of $1/2$ accounts for double counting, and the hopping rate coincides with the standard result for the phase-slip rate across a single Josephson junction of tunneling energy E_J and charging energy E_C [33]:

$$\Gamma = \frac{4}{\sqrt{\pi}}(8E_J^3 E_C)^{1/4} \exp\left(-\sqrt{\frac{8E_J}{E_C}}\right). \tag{B7}$$

Indeed, this is the phase-slip rate across a single KITE junction, because $E_L < \epsilon_L \ll E_J$. Note that we neglect the effect of double phase slips, that is, transitions $m_{\Sigma,\Delta} \to m_{\Sigma,\Delta} \pm 2$ with $m_{\Delta,\Sigma}$ unchanged.

Inspection of Eq. (B6) shows that, at all values of the external flux φ_{ext}, there are essentially two degenerate lowest rungs of potential wells at $m_\Delta = -1, 0$. This feature makes it possible to draw a zigzag path through the $\varphi_\Sigma \varphi_\Delta$ plane that connects all the relevant low-lying potential minima [see Fig. 2(c)]. To this end, we introduce a new tight-binding site index s and write the one-dimensional Hamiltonian

$$H_{n,\pi}^{\text{tight-binding,1D}} = \sum_{\{s\}} \frac{E_L \epsilon_L}{E_L + 2\epsilon_L}\left(s\pi + \frac{\pi}{2} + \varphi_{\text{ext}}\right)^2 |s\rangle\langle s|$$
$$- \sum_{\{s\}} \frac{1}{2}\Gamma(|s\rangle\langle s + 1| + |s + 1\rangle\langle s|), \tag{B8}$$

where the index $\{s\}$ again indicates summation over only the lowest potential minima. In the above, the most important feature is that neighboring sites are separated by a distance of π, rather than the conventional 2π. It is interesting to note that s in Eq. (B8) plays the role of a fluxon index, in the sense that transitions between

neighboring sites involve a single fluxon tunneling in or out of the KITE. Moreover, this Hamiltonian is formally identical to that of the usual Cooper-pair box under the interchange of Cooper-pair number with fluxon occupation. We therefore conclude that the regime of ground state delocalization—where the tight-binding approximation holds—is also the regime where the circuit begins to behave like a quantum phase-slip element [11].

We then observe that Eq. (B8) is also obtained from the continuous Hamiltonian in Eq. (6), where φ is the continuous analog of s, and so follows the degree of freedom φ_Σ. Because of the conjugacy between φ and N, as well as the correspondence from the previous section between ϕ and φ_Σ, we associate N with the number of Cooper pairs that have tunneled across the KITE. This model must be treated with caution; its spectrum is expected to resemble that of Eq. (B8) for only the lowest-energy eigenstates, and there are high-energy eigenstates of Eq. (6) that have no counterpart in Eq. (B8). As such, we present the eigenspectrum obtained by numerical diagonalization of H_π in Fig. 5(f) with no fitted parameters. Finally, in order to benchmark the ground state delocalization, we now define the effective amplitude of zero-point fluctuations of the superconducting phase [4] in Eq. (7).

3. Projection at $\theta_{\text{ext}} = 0$

Following the same procedure as in the previous section, we start with the Hamiltonian

$$H_{n,0} = 2E_C(N_\Sigma^2 + N_\Delta^2) + \frac{E_L \epsilon_L}{E_L + 2\epsilon_L}(\varphi_\Sigma + \varphi_{\text{ext}})^2$$
$$+ \epsilon_L \varphi_\Delta^2 - 2E_J \cos\varphi_\Sigma \cos\varphi_\Delta \tag{B9}$$

and observe that the relevant minima are located at $\varphi_\Sigma = m_\Sigma \pi$ and $\varphi_\Delta = m_\Delta \pi$, where m_Σ and m_Δ are again integers with the same parity. Here, we arrive the tight-binding Hamiltonian

$$H_{n,0}^{\text{tight-binding,2D}} = \sum_{\{m_\Sigma + m_\Delta \text{even}\}} \left[\frac{E_L \epsilon_L}{E_L + 2\epsilon_L} (m_\Sigma \pi + \varphi_{\text{ext}})^2 + \epsilon_L (m_\Delta \pi)^2 \right] |m_\Sigma, m_\Delta\rangle\langle m_\Sigma, m_\Delta|$$

$$- \sum_{\{m_\Sigma + m_\Delta \text{even}\}} \frac{1}{2}\Gamma(|m_\Sigma, m_\Delta\rangle\langle m_\Sigma \pm 1, m_\Delta \pm 1| + |m_\Sigma \pm 1, m_\Delta \pm 1\rangle\langle m_\Sigma, m_\Delta|), \tag{B10}$$

which crucially differs from Eq. (B6) in the $\pi/2$ offset equilibrium positions in the first line.

Examination of Eq. (B10) reveals that, at all values of the external flux φ_{ext}, there is a lowest rung of potential wells at $m_\Delta = 0$ and two degenerate next-lowest rungs at $m_\Delta = \pm 1$. Consequently, it is nontrivial to draw a one-dimensional path through the $\varphi_\Sigma \varphi_\Delta$ plane onto which to adequately project the dynamics, as we do at $\theta_{\text{ext}} = \pi$. Nonetheless, in order to model the lowest-energy transitions, we introduce the phenomenological one-dimensional Hamiltonian in Eq. (8). The energy spectrum obtained by numerical diagonalization of H_0, with parameters $\tilde{E}_J/h = 1.66$ GHz and $\tilde{E}_C/h = 1.48$ GHz determined by a fit to the data, is shown in Fig. 5(b). Here, φ is a collective degree of freedom that experiences the same parabolic confinement as the φ_Σ variable in Eq. (B9). As above, we define the effective amplitude of zero-point fluctuations of the phase in Eq. (9).

APPENDIX C: SPECTRUM FITTING

We fit the 12 measured transition frequencies shown in Figs. 5(c) and 5(d), and extracted from spectroscopy traces
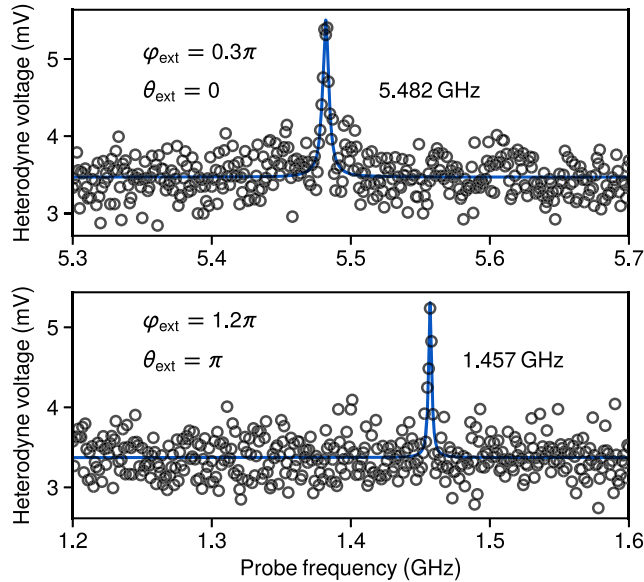

FIG. 6. Typical two-tone spectroscopy measurements, of the transition from the ground to fourth excited state at zero flux (top plot) and of that to the first excited state at half flux (bottom plot). Fitted Lorentzians are shown in blue.

like those in Fig. 6, to the eigenspectrum of Eq. (5). In total, this Hamiltonian has six parameters: E_J, E_C, E_L, ϵ_L, ϵ_C, and ϵ. We initialize our guess of E_J, E_L, and ϵ_L using normal resistance measurements and the Ambegaokar-Baratoff formula and start by setting ϵ to zero. Then, assuming a plasma frequency of 17.6 GHz, consistent with previous measurements in our laboratory at similar oxidation parameters, we infer E_C. In order to determine ϵ_C, which is mainly due to the capacitance of the metallic lines in the circuit, we run a finite-element simulation (Ansys HFSS) of the circuit, with all array junctions replaced by linear inductances and the two small junctions of the KITE replaced by capacitances. The simulation provides the frequency of a mode resembling the φ_Σ mode. We then numerically find ϵ_C—in a lumped element circuit corresponding to the HFSS model—that matches the simulated frequency, ultimately finding $\epsilon_C = 2.5$ GHz, which corresponds to a shunt capacitance of $C = 7.7$ fF.
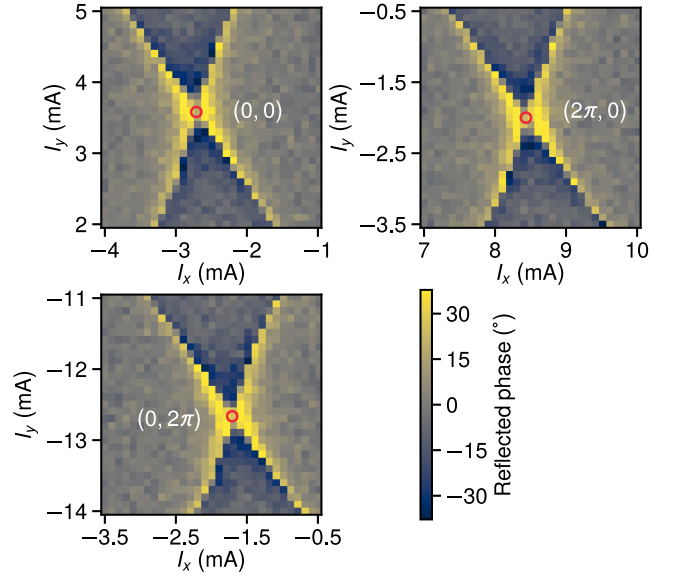

FIG. 7. Typical external flux calibration data. Phase of the reflected probe signal (color) on the readout port, at the fixed probe frequency of 5.580 GHz, as a function of both flux bias currents I_x and I_y. The three panels correspond to enlarged portions of Fig. 4(a), about the inversion-symmetric points $(\varphi_{\text{ext}}, \theta_{\text{ext}}) = (0, 0)$, $(2\pi, 0)$, and $(0, 2\pi)$. Red circles indicate symmetry points extracted using image inversion convolution and are used to fully determine the mapping from (I_x, I_y) onto $(\varphi_{\text{ext}}, \theta_{\text{ext}})$.
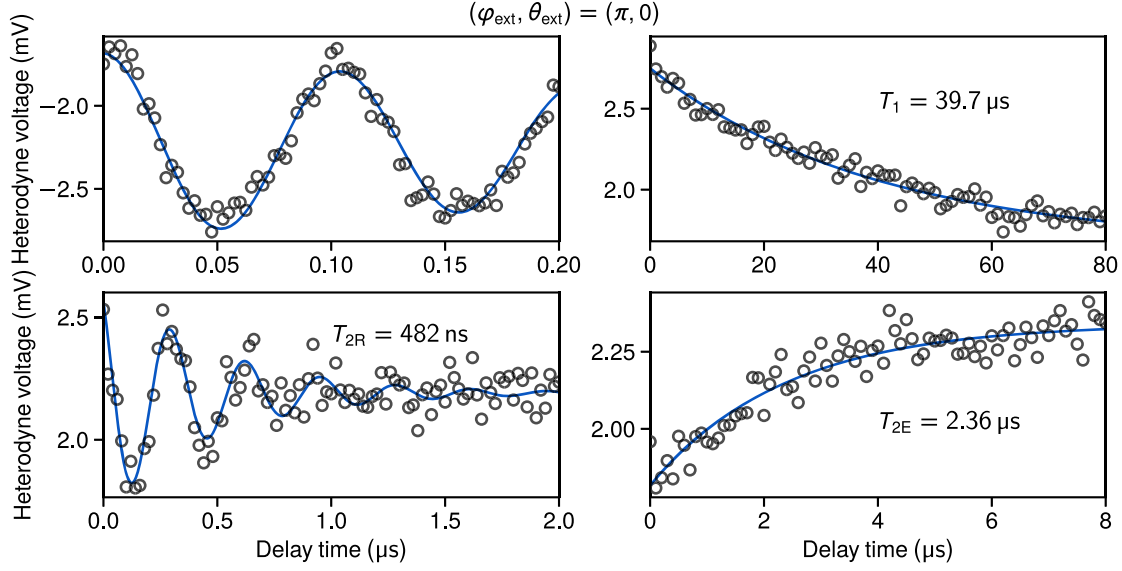
FIG. 8.   Time-domain measurements of the first excited state transition at $(\varphi_{\mathrm{ext}}, \theta_{\mathrm{ext}}) = (\pi, 0)$. Clockwise from top left: Rabi oscillations, relaxation, spin-echo decoherence, and Ramsey decoherence.

We use all these values to initialize a least-squares fit of the measured transition frequencies to fine-tune the four independent parameters E_J, E_C, E_L, and ϵ_L. Note that, as per the discussion in the main text, we do not expect every energy transition to be easily visible in our spectroscopic measurement setup through the readout mode, and, therefore, appropriate fitting requires a filtering of different energy levels. Indeed, the readout mode couples to the circuit through φ_Σ, and, therefore, in the fit routine, we neglect the transition to a given state $|i\rangle$ when $|\langle i|\varphi_\Sigma|g\rangle| \ll |\langle i|\varphi_\Delta|g\rangle|$. Finally, we improve the fit by ramping up the asymmetry parameter to $\epsilon = 0.03$, which corresponds to 6% relative asymmetry.

APPENDIX D: EXTERNAL FLUX CALIBRATION

We observe that the external magnetic flux drifts on the order of $0.02\Phi_0$, where $\Phi_0 = h/2e$ is the magnetic flux quantum, on a timescale of 24 h. Therefore, we calibrate the external magnetic flux axes φ_{ext} and θ_{ext} daily. To this end,

TABLE II.   Coherence properties at the four distinct two-dimensional external flux sweet spots for the first excited state transition. Here, χ denotes the dispersive shift on the readout resonator, T_1 denotes the relaxation time, T_{2R} denotes the Ramsey decoherence time, and T_{2E} denotes the spin-echo decoherence time.

$(\varphi_{\mathrm{ext}}, \theta_{\mathrm{ext}})$	$\omega_{ge}/2\pi$ (GHz)	χ (MHz)	T_1 (μs)	T_{2R} (μs)	T_{2E} (μs)
(0,0)	2.366	31	4.9	0.50	2.0
$(\pi, 0)$	0.792	−12	40	0.48	2.4
$(0, \pi)$	1.329	−30	16	0.43	4.0
(π, π)	1.460	−33	9.2	0.33	1.9

we monitor the readout resonator response as a function of I_x and I_y over a narrow range around three symmetry points, as shown in Fig. 7.

APPENDIX E: COHERENCE TIMES

In addition to the spectroscopy data shown in Figs. 5(c) and 5(d), we also measure the coherence times and dispersive shifts on the readout resonator by first calibrating a π pulse from measured Rabi oscillations (typical measurement and summary shown in Fig. 8 and Table II, respectively). The relatively large values of dispersive shift originate from the mutual inductance between the readout and circuit (shared junctions), which is designed to comprise a significant fraction of the readout resonator inductance. The relaxation times essentially follow a trend based on the transition frequency, suggesting that they are limited by dielectric loss. The small coherence times are likely due to flux noise exaggerated by the large loop sizes used in the circuit [see Fig. 3(b)]. This is consistent with the significant improvement in coherence time when adding a single echo pulse as well as the measured $T_{2R} < 0.1$ μs away from the sweet spots. We note that, although the sensitivity with respect to deviations in φ_{ext} changes substantially at the four sweet spots, the residual sensitivity with respect to θ_{ext} renders the overall susceptibility to flux noise roughly constant. Additionally, we suspect that phase slips in the array junctions might contribute to dephasing.

[1] J. Clarke, A. N. Cleland, M. H. Devoret, D. Esteve, and J. M. Martinis, *Quantum Mechanics of a Macroscopic Variable: The Phase Difference of a Josephson Junction*, Science **239**, 992 (1988).

[2] M. H. Devoret and R. J. Schoelkopf, *Superconducting Circuits for Quantum Information: An Outlook*, Science **339**, 1169 (2013).

[3] M. H. Devoret, in *Quantum Fluctuations*, Les Houches Session LXIII, edited by S. Reynaud, E. Giacobino, and J. Zinn-Justin (North-Holland, Amsterdam, 1997), pp. 351–386.

[4] S. M. Girvin, in *Quantum Machines: Measurement and Control of Engineered Quantum Systems*, Les Houches Session XCVI, edited by M. Devoret, B. Huard, R. Schoelkopf, and L. F. Cugliandolo (Oxford University, New York, 2014), pp. 113–256.

[5] M. Kjaergaard, M. E. Schwartz, J. Braumüller, P. Krantz, J. I.-J. Wang, S. Gustavsson, and W. D. Oliver, *Superconducting Qubits: Current State of Play*, Annu. Rev. Condens. Matter Phys. **11**, 369 (2020).

[6] D. Gottesman, A. Kitaev, and J. Preskill, *Encoding a Qubit in an Oscillator*, Phys. Rev. A **64**, 012310 (2001).

[7] A. Kitaev, *Protected Qubit Based on a Superconducting Current Mirror*, arXiv:cond-mat/0609441.

[8] B. Douçot and L. B. Ioffe, *Physical Implementation of Protected Qubits*, Rep. Prog. Phys. **75**, 072001 (2012).

[9] P. Brooks, A. Kitaev, and J. Preskill, *Protected Gates for Superconducting Qubits*, Phys. Rev. A **87**, 052306 (2013).

[10] J. Cohen, W. C. Smith, M. H. Devoret, and M. Mirrahimi, *Degeneracy-Preserving Quantum Nondemolition Measurement of Parity-Type Observables for Cat Qubits*, Phys. Rev. Lett. **119**, 060503 (2017).

[11] J. E. Mooij and Y. V. Nazarov, *Superconducting Nanowires as Quantum Phase-Slip Junctions*, Nat. Phys. **2**, 169 (2006).

[12] F. Piquemal and G. Genevès, *Argument for a Direct Realization of the Quantum Metrological Triangle*, Metrologia **37**, 207 (2000).

[13] V. E. Manucharyan, J. Koch, L. I. Glazman, and M. H. Devoret, *Fluxonium: Single Cooper-Pair Circuit Free of Charge Offsets*, Science **326**, 113 (2009).

[14] T. M. Hazard, A. Gyenis, A. Di Paolo, A. T. Asfaw, S. A. Lyon, A. Blais, and A. A. Houck, *Nanowire Superinductance Fluxonium Qubit*, Phys. Rev. Lett. **122**, 010504 (2019).

[15] L. Grünhaupt, M. Spiecker, D. Gusenkova, N. Maleeva, S. T. Skacel, I. Takmakov, F. Valenti, P. Winkel, H. Rotzinger, W. Wernsdorfer, A. V. Ustinov, and I. M. Pop, *Granular Aluminium as a Superconducting Material for High-Impedance Quantum Circuits*, Nat. Mater. **18**, 816 (2019).

[16] M. Pita-Vidal, A. Bargerbos, C.-K. Yang, D. J. van Woerkom, W. Pfaff, N. Haider, P. Krogstrup, L. P. Kouwenhoven, G. de Lange, and A. Kou, *Gate-Tunable Field-Compatible Fluxonium*, Phys. Rev. Applied **14**, 064038 (2020).

[17] M. Peruzzo, A. Trioni, F. Hassani, M. Zemlicka, and J. M. Fink, *Surpassing the Resistance Quantum with a Geometric Superinductor*, Phys. Rev. Applied **14**, 044055 (2020).

[18] I. V. Pechenezhskiy, R. A. Mencia, L. B. Nguyen, Y.-H. Lin, and V. E. Manucharyan, *The Superconducting Quasicharge Qubit*, Nature (London) **585**, 368 (2020).

[19] B. Douçot and J. Vidal, *Pairing of Cooper Pairs in a Fully Frustrated Josephson-Junction Chain*, Phys. Rev. Lett. **88**, 227005 (2002).

[20] L. B. Ioffe and M. V. Feigel'man, *Possible Realization of an Ideal Quantum Computer in Josephson Junction Array*, Phys. Rev. B **66**, 224503 (2002).

[21] G. Blatter, V. B. Geshkenbein, and L. B. Ioffe, *Design Aspects of Superconducting-Phase Quantum Bits*, Phys. Rev. B **63**, 174511 (2001).

[22] S. Gladchenko, D. Olaya, E. Dupont-Ferrier, B. Doucot, L. B. Ioffe, and M. E. Gershenson, *Superconducting Nanocircuits for Topologically Protected Qubits*, Nat. Phys. **5**, 48 (2009).

[23] V. E. Manucharyan, *Superinductance*, Ph.D. thesis, Yale University, 2012.

[24] W. C. Smith, A. Kou, X. Xiao, U. Vool, and M. H. Devoret, *Superconducting Circuit Protected by Two-Cooper-Pair Tunneling*, npj Quantum Inf. **6**, 8 (2020).

[25] M. T. Bell, J. Paramanandam, L. B. Ioffe, and M. E. Gershenson, *Protected Josephson Rhombus Chains*, Phys. Rev. Lett. **112**, 167001 (2014).

[26] A. Gyenis, P. S. Mundada, A. Di Paolo, T. M. Hazard, X. You, D. I. Schuster, J. Koch, A. Blais, and A. A. Houck, *Experimental Realization of a Protected Superconducting Circuit Derived from the 0-π Qubit*, PRX Quantum **2**, 010339 (2021).

[27] W. C. Smith, A. Kou, U. Vool, I. M. Pop, L. Frunzio, R. J. Schoelkopf, and M. H. Devoret, *Quantization of Inductively Shunted Superconducting Circuits*, Phys. Rev. B **94**, 144507 (2016).

[28] N. A. Masluk, I. M. Pop, A. Kamal, Z. K. Minev, and M. H. Devoret, *Microwave Characterization of Josephson Junction Arrays: Implementing a Low Loss Superinductance*, Phys. Rev. Lett. **109**, 137002 (2012).

[29] H. Zhang, S. Chakram, T. Roy, N. Earnest, Y. Lu, Z. Huang, D. K. Weiss, J. Koch, and D. I. Schuster, *Universal Fast-Flux Control of a Coherent, Low-Frequency Qubit*, Phys. Rev. X **11**, 011010 (2021).

[30] Although we neglect the readout mode in Eq. (5), we note that it directly couples to the ϕ mode exclusively. Since the ϕ variable hybridizes significantly with φ_Σ, but not φ_Δ, we expect only a subset of the eigenstates to dispersively shift the readout resonance at external flux values where φ_Σ and φ_Δ are roughly independent. This is the case at $\theta_{\text{ext}} = 0$ but not $\theta_{\text{ext}} = \pi$.

[31] D. T. Le, A. Grimsmo, C. Müller, and T. M. Stace, *Doubly Nonlinear Superconducting Qubit*, Phys. Rev. A **100**, 062321 (2019).

[32] P. Groszkowski, A. D. Paolo, A. L. Grimsmo, A. Blais, D. I. Schuster, A. A. Houck, and J. Koch, *Coherence Properties of the 0-π Qubit*, New J. Phys. **20**, 043053 (2018).

[33] K. A. Matveev, A. I. Larkin, and L. I. Glazman, *Persistent Current in Superconducting Nanorings*, Phys. Rev. Lett. **89**, 096802 (2002).